Ocean Science

Spatial and temporal variability of solar penetration depths in the Bay of Bengal and its impact on sea surface temperature (SST) during the summer monsoon

Jack Giddings[1], Karen J. Heywood[1], Adrian J. Matthews[2], Manoj M. Joshi[1], Benjamin G. M. Webber[1], Alejandra Sanchez-Franks[3], Brian A. King[3], and Puthenveettil N. Vinayachandran[4]

[1]Centre for Ocean and Atmospheric Sciences, School of Environmental Sciences,
University of East Anglia, Norwich, NR4 7TJ, UK
[2]Centre for Ocean and Atmospheric Sciences, School of Environmental Sciences and School of Mathematics,
University of East Anglia, Norwich, NR4 7TJ, UK
[3]National Oceanography Centre, Southampton, SO14 3ZH, UK
[4]Center for Atmospheric and Oceanic Sciences, Indian Institute of Science, Bengaluru, India

Correspondence: Karen J. Heywood (k.heywood@uea.ac.uk)

Abstract. Chlorophyll has long been known to influence air–sea gas exchange and CO_2 drawdown. But chlorophyll also influences regional climate through its effect on solar radiation absorption and thus sea surface temperature (SST). In the Bay of Bengal, the effect of chlorophyll on SST has been demonstrated to have a significant impact on the Indian summer (southwest) monsoon. However, little is known about the drivers and impacts of chlorophyll variability in the Bay of Bengal during the southwest monsoon. Here we use observations of downwelling irradiance measured by an ocean glider and three profiling floats to determine the spatial and temporal variability of solar absorption across the southern Bay of Bengal during the 2016 summer monsoon. A two-band exponential solar absorption scheme is fitted to vertical profiles of photosynthetically active radiation to determine the effective scale depth of blue light. Scale depths of blue light are found to vary from 12 m during the highest (0.3–0.5 mg m^{-3}) mixed-layer chlorophyll concentrations to over 25 m when the mixed-layer chlorophyll concentrations are below 0.1 mg m^{-3}. The Southwest Monsoon Current and coastal regions of the Bay of Bengal are observed to have higher mixed-layer chlorophyll concentrations and shallower solar penetration depths than other regions of the southern Bay of Bengal. Substantial sub-daily variability in solar radiation absorption is observed, which

highlights the importance of near-surface ocean processes in modulating mixed-layer chlorophyll. Simulations using a one-dimensional K-profile parameterization ocean mixed-layer model with observed surface forcing from July 2016 show that a 0.3 mg m^{-3} increase in chlorophyll concentration increases sea surface temperature by 0.35 °C in 1 month, with SST differences growing rapidly during calm and sunny conditions. This has the potential to influence monsoon rainfall around the Bay of Bengal and its intraseasonal variability.

1 Introduction

Absorption of incoming solar radiation at the ocean surface modulates the upper-ocean heat content, which controls the exchange of heat and moisture to the lower troposphere (Zaneveld et al., 1981; Lewis et al., 1990). Water containing chlorophyll absorbs more solar irradiance than clear water, modifying the vertical heating profile of the upper ocean and thus sea surface temperature (SST; Morel, 1988; Morel and Antoine, 1994; Ohlmann, 2003), which in turn can affect the large-scale ocean circulation and climate (Sweeney et al., 2005; Wetzel et al., 2006).

The concentration of chlorophyll in the Indian Ocean has been shown to have a significant effect on the South Asian

monsoon (Nakamoto et al., 2000; Wetzel et al., 2006; Turner et al., 2012; Giddings et al., 2020). Imposing seasonally varying chlorophyll concentrations in the Bay of Bengal (BoB) has been found to increase SST by 0.5 °C, which can increase rainfall by up to 3 mm d^{-1} over Myanmar during the South Asian summer (southwest) monsoon onset and over northeastern India and Bangladesh during the autumn intermonsoon period (Giddings et al., 2020). In the Arabian Sea, the inclusion of seasonally varying chlorophyll due to phytoplankton blooms in a coupled climate model led to a 50 % reduction in mixed-layer depth (MLD) biases, an increase in local SST, and a subsequent increase in rainfall of up to 2 mm d^{-1} over western India during the southwest monsoon onset (Turner et al., 2012). Chlorophyll concentrations of 0.3 mg m^{-3} in the Arabian Sea during boreal spring have been found to increase SST by 0.4 °C compared with simulations using globally constant attenuation rates corresponding to near-zero chlorophyll concentrations in an ocean isopycnal general circulation model (GCM; Nakamoto et al., 2000). Coupling a biogeochemistry model to a coupled ocean–atmosphere GCM to derive chlorophyll-dependent attenuation rates of solar radiation led to an SST increase of 1 °C in the Arabian Sea during autumn and an increase in summer monsoon rainfall of 3 mm d^{-1} along the west coast of India (Wetzel et al., 2006). However, little is known about the influence of surface chlorophyll on the temporal and spatial variability of solar penetration depths across the BoB and how surface chlorophyll directly impacts SST during the summer southwest monsoon.

Remote sensing of chlorophyll pigments from satellites has demonstrated that chlorophyll concentrations vary substantially in both space and time, suggesting a corresponding spatial and temporal variability of solar penetration depth (Nakamoto et al., 2000; Murtugudde et al., 2002). Chlorophyll-dependent optical parameters such as the diffuse attenuation coefficient (K_d), defined as the fraction of solar radiation attenuated per unit distance through the upper ocean, can be determined from in situ radiometer measurements (e.g. Smith and Baker, 1981) and estimated using ocean colour data from satellites (e.g. Lee et al., 2005).

Previous studies have parameterized solar penetration depths as a function of remotely sensed chlorophyll concentration for certain solar absorption schemes. Morel and Antoine (1994) produced high-order polynomial relationships for a two-band model that related the scale depths of blue and red light (300–750 nm) to the surface chlorophyll concentration, assuming an idealized Gaussian vertical profile of chlorophyll to a depth of 1 solar penetration depth. Ohlmann (2003) used the HYDROLIGHT radiative transfer model (Ohlmann and Siegel, 2000) to produce vertical profiles of solar radiation for pre-defined chlorophyll concentrations, time of day, and cloud cover to determine optical parameters. A scale depth relationship was developed for the transmission of the ultraviolet–visible spectrum (300–750 nm) as part of a two-band model. However, there is re-

maining uncertainty over which of these parameterizations is most applicable for use in a specific region or climate model.

The oceanic components of state-of-the-art GCMs have various chlorophyll-dependent parameterizations and associated solar absorption schemes. For example, the Community Earth System Model (CESM; Kay et al., 2015) uses the Ohlmann (2003) chlorophyll-dependent parameterization for a two-band model (Smith et al., 2010). Meanwhile, the Institute Pierre Simon Laplace climate model (IPSL; Mignot et al., 2013) uses a three-band model with which light is split into red, green, and blue wavebands, each with a chlorophyll-dependent attenuation coefficient (Lengaigne et al., 2007). Both GCMs have the capability to assimilate satellite-derived chlorophyll concentrations. These chlorophyll concentrations can then be converted into a solar penetration depth using chlorophyll-dependent parameterizations. Satellite-derived chlorophyll concentrations have revolutionized our understanding of how chlorophyll-induced heating affects ocean dynamics and the climate system (Murtugudde et al., 2002; Sweeney et al., 2005; Wetzel et al., 2006). However, the limited spatial and temporal resolution of these GCMs and assimilated ocean colour data mean they inadequately resolve mesoscale and sub-seasonal chlorophyll concentration variability, which might influence the intraseasonal variability of BoB SST and the South Asian summer monsoon.

Across the southern BoB, the seasonal reversal of wind direction during the boreal summer creates conditions conducive for chlorophyll blooms. Southwesterly monsoon winds initiate the Southwest Monsoon Current (SMC), which flows northeastward, advecting cooler, saline water from the Arabian Sea and the western equatorial Indian Ocean around the southernmost point of India and Sri Lanka into the warmer and fresher BoB (Fig. 1b; Jensen, 2003; Sanchez-Franks et al., 2019). The SMC evolves into a shallow, narrow, and fast-moving current with surface speeds of up to 0.6 m s^{-1} and a thickness of up to 550 m (Webber et al., 2018). Large chlorophyll blooms along the southwestern coastal shelf of India, initiated by upwelling nutrients, become entrained in the SMC and are advected around the south of Sri Lanka into the central BoB in summer (Lévy et al., 2007). A tongue of high surface chlorophyll concentrations extends into the central BoB, following the path of the SMC (Fig. 1a). The bloom is sustained east of Sri Lanka in the cyclonic eddy of the Sri Lanka Dome (SLD), identified as a region of lower absolute dynamic topography and cyclonic current vectors in Fig. 1b. Open-ocean Ekman upwelling in the SLD brings nutrients to the near-surface to support the phytoplankton population (Vinayachandran and Yamagata, 1998; Vinayachandran et al., 2004; Thushara et al., 2019). Hence, the high surface chlorophyll concentrations associated with the SMC and SLD are expected to lead to reduced solar penetration depths throughout the summer monsoon period.
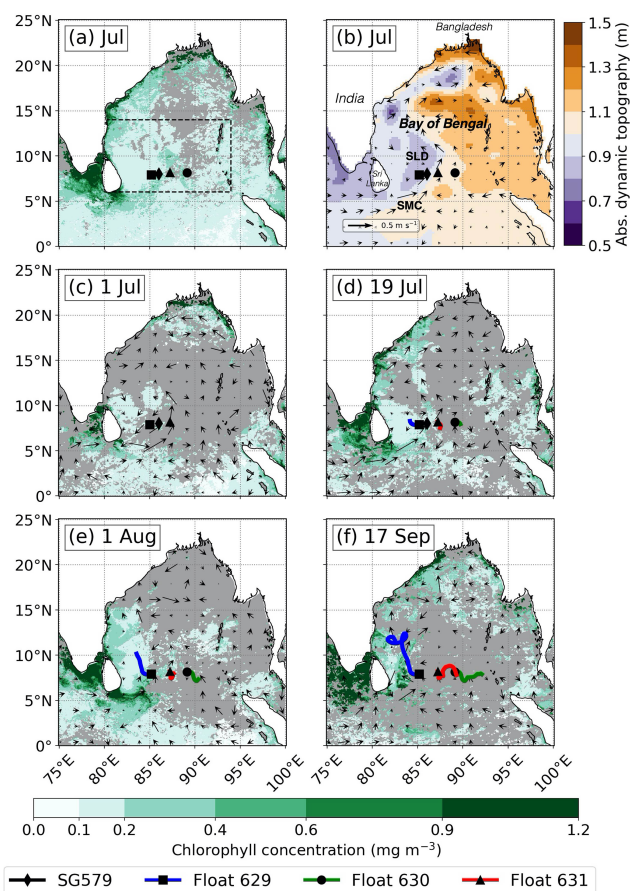
Figure 1. (a) Satellite composite of July 2016 average 4 km chlorophyll *a* concentration (mg m^{-3}) obtained from ESA OC-CCI version 3.1. The dashed black box shows the outline of Fig. 5a. **(b)** Absolute dynamic topography (m) of horizontal resolution (0.25° × 0.25°) overlaid with surface geostrophic velocity (m s^{-1}) from AVISO for July 2016. **(c–f)** Satellite composite of 8-daily averaged 4 km chlorophyll *a* concentration and surface geostrophic velocities for 1–8, 19–27 July, 1–8 August, and 17–25 September. Deployment locations and trajectories of glider SG579 (diamond marker; black line), float 629 (square marker; blue line), float 630 (circle marker; green line), and float 631 (triangle marker; red line) are overlaid. Missing data are shaded grey.

The large freshwater flux from river output and rainfall in the BoB during boreal summer creates a barrier layer wherein strong salinity stratification forms within the isothermal layer and below the mixed layer (Vinayachandran et al., 2002; Sengupta et al., 2016). The presence of the barrier layer isolates the mixed layer above from cooling by entrainment (Duncan and Han, 2009). Instead, the surface heat flux forcing, such as shortwave radiation and turbulent heat fluxes, primarily controls the warming and cooling phases of the surface ocean (Li et al., 2017). The barrier layer has been found to influence BoB SST (Drushka et al., 2014) and its thickness impacts the summer monsoon intraseasonal oscillation (Li et al., 2017). The additional effects of localized bi-

ological heating from surface chlorophyll could amplify the warming in these shallow mixed layers. Understanding the mesoscale and sub-seasonal solar penetration depth variability and its impact on BoB surface ocean properties would highlight the direct effect of chlorophyll concentration at finer spatial and temporal scales.

In this study, we determine (i) how solar penetration depth varies temporally and spatially across the southern BoB, (ii) how near-surface chlorophyll concentrations affect solar penetration depths, and (iii) how chlorophyll concentration directly impacts SST in the southern BoB. To quantify the influence of chlorophyll on solar penetration depth and SST, an ocean glider and three profiling floats were deployed as part of the joint India–UK Bay of Bengal Boundary Layer Experiment (BoBBLE; Vinayachandran et al., 2018) to measure in situ physical, optical, and biogeochemical variables in the upper ocean during July 2016 at high horizontal and temporal resolution. We fit a two-band solar absorption function to observed vertical profiles of photosynthetically active radiation (PAR). PAR is an integral of downwelling irradiance between 400 and 700 nm (blue to red light), allowing us to determine the downward penetration of solar radiation, as represented by the length scale associated with the absorption of blue light, which is represented by the parameter h_2.

An overview of the data and methods is presented in Sect. 2. Section 3 presents an analysis of the temporal and spatial variability of determined h_2 (Sect. 3.1), as well as a comparison of determined h_2 and observed chlorophyll concentration to two previously published parameterizations (Sect. 3.2). This is then followed by an analysis of five idealized simulations with an imposed solar penetration depth from the h_2 observations to investigate the impact of observed chlorophyll on upper-ocean radiant heating rate and SST in the southern BoB. The simulations were conducted using the one-dimensional K-profile parameterization ocean mixed-layer model (Sect. 3.3). Section 4 presents the discussion and conclusions.

2 Data and methods

2.1 Observations and instruments

2.1.1 Ocean gliders and Argo profiling floats

During the BoBBLE field campaign (Vinayachandran et al., 2018), a Seaglider (SG579) was deployed at 86° E on 30 June 2016 along a transect at 8° N east of Sri Lanka and piloted to 85.3° E by 8 July, where the glider continued to take measurements until 29 July 2016. The glider profiled on a sawtooth trajectory from the surface to 700–1000 m, completing a full dive cycle approximately every 4 h. The glider was equipped with a Sea-Bird Electronics (SBE) conductivity (salinity), temperature, and depth (CTD) sensor, a Wetlabs Triplet Ecopuck measuring chlorophyll *a* fluorescence

and optical backscatter at wavelengths 470 and 700 nm, and a Biospherical Instruments quantum scalar irradiance PAR ($\mu E\,m^{-2}\,s^{-1}$) sensor measuring visible wavelengths between 400 and 700 nm. The Wetlabs and PAR sensors sampled to a depth of 300 m with a vertical resolution of ~ 1 m. Quality control was performed on the entire conductivity–temperature (CT) dataset using conservative temperature–absolute salinity (IOC et al., 2010) space analysis and further quality control in depth space for individual vertical profiles. Salinity spikes were removed when the glider vertical speed was less than $0.035\,m\,s^{-1}$ as the unpumped CT sensor relied on a suitable flow of water for reliable measurements. The ocean glider PAR measurements were factory-calibrated. The CT sensor was factory-calibrated and was then further calibrated against in situ ship CTD observations.

Argo profiling floats 629, 631, and 630 that are part of the international Argo float programme were deployed along the $8°$ N transect at 85.5, 87, and $89°$ E on 28 June, 1 July, and 4 July, respectively; they sampled to 500 m daily until mid-August and every other day until the end of September. All three floats were equipped with an SBE 41N CTD and a Satlantic OCR-504 ICSW radiometer measuring downwelling irradiance at wavelengths 380, 490, and 555 nm ($\mu W\,cm^{-2}\,nm^{-1}$) as well as PAR ($\mu E\,m^{-2}\,s^{-1}$). The CTD measurements were factory-calibrated, and radiometer measurements were factory-calibrated with channel-specific coefficients. The vertical resolution on the ascent to the surface was ~ 1 m for the radiometer and CTD.

2.1.2 PAR

All night-time PAR profiles (local solar zenith angles greater than $70°$) and low-light PAR profiles (maximum PAR in the top 5 m is less than $100\,\mu E\,m^{-2}\,s^{-1}$) measured by the glider and profiling floats were discarded. Further quality control was carried out to remove the effect of external environmental factors, which include shading by passing clouds that causes sudden fluctuations in light intensity and wave focusing that creates sawtooth spiking in the vertical PAR profiles (Zaneveld et al., 2001). All PAR data between 0 and 5 m of depth were removed from the analysis, as noise from wave focusing obscured the signal of the absorption of solar radiation. A quality control method using a fourth-degree polynomial, modified from the methodology of Organelli et al. (2016), was used to identify PAR perturbations below the near-surface and remove profiles displaying excessive noise.

2.1.3 Chlorophyll

The glider's raw fluorescence voltages were converted into chlorophyll a concentrations according to the manufacturer calibrations. Since phytoplankton that are exposed to too much sunlight trigger the non-photochemical quenching mechanism to protect themselves from photooxidative damage (Müller et al., 2001), chlorophyll a fluorescence

is suppressed near the surface in the daytime. To correct for quenching, night-time fluorescence-to-backscatter ratios were used to derive corrected daytime chlorophyll a fluorescence profiles (Thomalla et al., 2018). The glider fluorescence-derived chlorophyll a concentrations, after correcting for non-photochemical quenching, showed values that were higher than those derived from the shipboard CTD chlorophyll a fluorescence sensor. Concentrations were calibrated by applying a scale factor and offset derived using linear regression between the glider and CTD chlorophyll a profiles.

The profiling floats did not make chlorophyll a fluorescence measurements, so a novel approach was developed to derive chlorophyll a concentration from radiometer data alone (see Appendix A for method details). Chlorophyll a strongly absorbs light at the 490 nm wavelength, so the vertical gradient of $E_d(490)$, which is the downwelling radiation flux at 490 nm, was used to derive a proxy for the in situ chlorophyll a concentration to identify the vertical distribution of chlorophyll a. Vertical profiles of the natural log of $E_d(490)$ were individually corrected for their mean in situ dark count calculated from measurements below 200 m (Organelli et al., 2016). Profiles displaying excessive noise were eliminated using the fourth-degree polynomial method of Organelli et al. (2016). The attenuation coefficient K_d was calculated for each 1 m discretized layer. The attenuation coefficient K_d is the sum of the attenuation of pure seawater (K_w), represented as a constant, and the attenuation due to biology (K_{bio}), a chlorophyll a component (Morel and Maritorena, 2001; Xing et al., 2011). Further quality control is applied to vertical profiles of K_{bio} before chlorophyll a is calculated using empirically determined coefficients from Morel et al. (2007) (Fig. A1 in the Appendix). The chlorophyll a pigment concentration that was derived from radiometry data or remotely sensed by satellite will henceforth be referred to as "chlorophyll" for convenience.

2.1.4 Satellite products

The remotely sensed chlorophyll concentrations used in this study are sourced from the European Space Agency's Ocean Colour–Climate Change Initiative (ESA OC-CCI; Lavender et al., 2015) version 3.1 (available at http://www.esa-oceancolour-cci.org, last access: 4 July 2018). The OC-CCI project involved the merging of remotely sensed chlorophyll concentrations from MODIS, MERIS, SeaWiFS, and VIIRS radiance sensors to provide a continuous dataset from 1997–2016 with increased spatial coverage of the global oceans. The radiance sensors on the satellites detect the water-leaving radiance at specific wavelengths to estimate chlorophyll concentration. The thickness of the ocean surface layer "seen" by the radiance sensors is approximately 1 solar penetration depth or the depth at which downwelling irradiance decreases to $1/e$ of the surface irradiance (Gordon and McCluney, 1975), depending on the local chloro-

phyll concentrations. The 8 d merged and monthly composites of chlorophyll concentration with spatial resolutions of 4 km have been used to investigate the weekly and monthly variability of the chlorophyll concentration influencing solar penetration depths in the deployment region across the southern BoB from July to September 2016.

Satellite-derived absolute geostrophic velocities (meridional and zonal components) and absolute dynamic topography are altimeter products produced by SSALTO/Duacs, distributed by AVISO (https://www.aviso.altimetry.fr, last access: 15 August 2018), and are available through the Copernicus Marine Environment Monitoring Service (http://marine.copernicus.eu, last access: 15 August 2018). The daily composites of absolute geostrophic velocities and absolute dynamic topography have a spatial resolution of 0.25° × 0.25° and are used to investigate the surface current velocities that control chlorophyll concentration advection from July to September 2016.

2.2 Methods

The penetration depth of solar radiation is frequency-dependent, with higher frequencies ("blue" light) having a much larger penetration depth than lower frequencies ("red" light). A double exponential function (Paulson and Simpson, 1977) can be used to parameterize this behaviour in ocean models (e.g. Sweeney et al., 2005) and in mixed-layer heat budget studies (e.g. Vialard et al., 2008; Girishkumar et al., 2017). For this study we use a double exponential function of the form

$$Q(z) = q_2 \left[\left(\frac{R}{1-R} \right) e^{-\frac{z}{h_1}} + e^{-\frac{z}{h_2}} \right] + d, \qquad (1)$$

where Q (W m^{-2}) is the irradiance at depth z (m). Surface irradiance just below the ocean surface for blue light is denoted by q_2 (W m^{-2}). The scale depths, h_1 and h_2, represent the e-folding depths (m) of absorption of red and blue light, respectively. The parameter R is the ratio of the flux of red light to the total and is a measure of the partition of the solar flux into the arbitrary red and blue bands. An offset d (W m^{-2}) has also been introduced to allow for a non-zero instrument response at zero radiation flux when applied to a radiometer. In practice, d is very small (compared with q_2).

Paulson and Simpson (1977) determined the optical parameters (R, h_1, and h_2) for each of the five Jerlov water types, which represent the range of turbidity observed in open-ocean water (Jerlov, 1968). Water type I represents low open-ocean chlorophyll concentrations of 0 to 0.01 mg m^{-3} (Morel, 1988), with h_1 and h_2 of 0.35 and 23 m, respectively. Water type III represents high open-ocean chlorophyll concentrations of 1.5 to 2.0 mg m^{-3} (Morel, 1988), with h_1 and h_2 of 1.4 and 7.9 m, respectively. The scale depth of blue light ($h_2 \sim 20$ m) is much larger than that for red light ($h_1 \sim 1$ m), and hence variations in h_2 exert the main control on
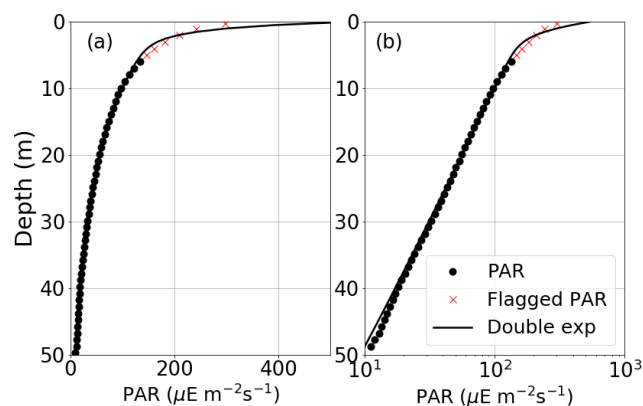
Figure 2. (a) Profile of PAR (black circles) measured from float 629 from the surface to 50 m of depth with a fitted double exponential function (black line) to PAR between 5 and 100 m of depth. R and h_1 were specified to be 0.67 and 1.0 m, respectively. Red crosses show flagged PAR values that were excluded from the curve fit. **(b)** Same vertical profile of PAR and fitted double exponential function as **(a)**, but presented in log space.

the radiant heating of the surface ocean mixed layer and thus SST.

Optical parameter R is 0.58 in water type I and 0.78 in water type III. The two-band model is an arbitrary approximation of the full solar spectrum, and there is no a priori definition of the value of the cut-off frequency between the red and blue bands. Hence, the parameter R is allowed to vary, along with h_2, to maximize the fit of the two-band model to the data. The variation of R should not be interpreted as a physical change in the fraction of red light at the surface, which of course is independent of the ocean conditions below. Instead, the variation of R should be interpreted as a degree of freedom in fitting a simple two-band scheme to model the full solar spectrum.

In this study we use Eq. (1) to fit to profiles of PAR reported in terms of moles of photons (µE m^{-2} s^{-1}) instead of units of energy (W m^{-2}). For PAR measurements, the conversion of units from µE m^{-2} s^{-1} to W m^{-2} can only be an approximation as the PAR instrument measures photons across a range of visible wavelengths, but the exact spectrum across that range is unknown at any particular time (Sager and McFarlane, 1997). Although the absolute values of PAR change with unit conversion, the attenuation rate of visible light with depth and thus the value of h_2 are independent of the unit conversion of PAR. Hence, in practice we fit Eq. (1) to profiles of PAR with units of µE m^{-2} s^{-1} to determine values of h_2 and avoid PAR conversion uncertainty.

From the excessively noisy 1 m vertical resolution PAR measurements close to the surface, we are unable to determine the transmission of red light (values of R and h_1). We assume Jerlov water type IB (Paulson and Simpson, 1977) to be applicable to our region based upon initial determinations of $h_2 \sim 17$ m from fitting Eq. (1). We therefore con-

strain R to be 0.67 and h_1 to be 1 m and thus fit PAR profiles between 5 and 100 m to the transmission of blue light with depth (h_2) using Eq. (1) (Fig. 2a). The same fit plotted in log space (Fig. 2b) results in a nearly straight line below 5 m, demonstrating that the decrease in PAR can be approximately represented with a single exponential below this depth. Generally, flagged PAR values in the top 5 m depart from the fit due to excessive noise caused by wave focusing and cloud shadows, as well as the poor approximation of Eq. (1) representing the absorption of longer wavelengths near the surface. The contribution of the fixed parameters used for the fit was estimated by varying R and h_1 between Jerlov water types I and III from Paulson and Simpson (1977) and varying the depth of removed near-surface PAR between 3 and 7 m. We combine the maximum and minimum values of each source of uncertainty to calculate the upper and lower uncertainty bounds of each derived value of h_2.

3 Results

3.1 Glider and profiling float observations

The SLD is a prominent feature in the southwest BoB during the summer monsoon and is typically associated with high surface chlorophyll concentrations (Thushara et al., 2019). At the start of July 2016, the SLD is centred around 85–86° E and 5–10° N to the west of the SMC (Fig. 1b). Glider SG579 is located inside the SLD from 30 June and observes the weakening of this cyclonic eddy after 2 July, remaining in a localized region between 85 and 86° E (Fig. 1c; black diamond). The average mixed-layer salinity and temperature are 34.0 ± 0.4 g kg^{-1} and 28.0 ± 0.2 °C, respectively (Fig. 3a and b). Chlorophyll concentrations peak on 1 July with values of 0.8 mg m^{-3} at a depth of 18 m, indicating high surface chlorophyll concentrations (Fig. 3d). Corresponding values of h_2 decrease from an average of 16 ± 2 m on 30 June to 13 ± 1 m on 1 July, as the average 0–30 m chlorophyll concentration (henceforth referred to as Chl a_{30}) increases from 0.3 ± 0.1 to 0.5 ± 0.1 mg m^{-3} in 1 d (Fig. 3d; black circles).

After 2 July, the SLD weakens and shifts towards the northwest, but the SMC continues to flow into the south–central BoB. Patches of surface chlorophyll, with concentrations of 0.1–0.4 mg m^{-3} (Fig. 1d), continue to be advected by the SMC into the region where glider SG579 is parked at a virtual mooring at 85° E until 19 July. Within the SMC, the mixed layer warms from 28.0 to 29.0 ± 0.2 °C and freshens from 34.0 to 33.3 ± 0.1 g kg^{-1} (Fig. 3a and b). Chlorophyll concentrations below the mixed layer remain around 0.5 mg m^{-3}, forming a deep chlorophyll maximum between 30 and 50 m of depth (Fig. 3d). Meanwhile, average Chl a_{30} decreases to less than 0.2 ± 0.1 mg m^{-3} (Fig. 3d) and the corresponding average values of h_2 increase to more than 20 ± 2 m until 16 July (Fig. 4a; dashed black line). The position and velocity of the SMC relative to the biologically pro-

ductive southern coast of Sri Lanka and southwest coast of India determines how much surface chlorophyll is entrained and advected into the south–central BoB (Vinayachandran et al., 2004). Throughout most of July the SMC is too far south to intercept the high surface chlorophyll concentrations along the southern coast of Sri Lanka (Fig. 1d), explaining why in situ surface chlorophyll concentrations are relatively low after 2 July (Fig. 3d). The temporal variability of h_2 in the SMC is large, with a standard deviation of 4 m (Fig. 4a). Values ranged between 15 and 31 m from 4 July onwards, which we partly attribute to sub-daily temporal variability in the mixed-layer and surface chlorophyll concentrations. However, the derived h_2 values from glider SG579 are associated with relatively high uncertainty (typically ± 2 m) due to the fitting of the double exponential function to noisy vertical PAR profiles, which may contribute to this apparent variability.

The profiling float dataset allows us to extend the glider dataset temporally and spatially, providing daily measurements of solar penetration depths until mid-August and then measurements every 2 d until the end of September, spanning much of the southern BoB. The vertical profiles of downwelling irradiance measured from the profiling floats are less noisy than those measured from the glider. Hence, the profiling floats display lower uncertainty in determined values of h_2 when compared with the glider (Fig. 4a–d). As the SMC flows northeastward into the south–central BoB during early July, the surface current bifurcates. The main branch flows northward towards 10° N, and the smaller branch flows eastward towards 90° E (Fig. 1d). Figure 5b shows the longitudinal variations of h_2 across the SLD and SMC. Values of h_2 decrease as remotely sensed chlorophyll concentrations increase towards the centre of the SMC (Fig. 5a and b), consistent with previous studies that show the SMC increasing chlorophyll concentrations in the region (e.g. Vinayachandran et al., 2004; Thushara et al., 2019). Float 631 is deployed on the eastern flank of the SMC and completes an anticyclonic loop, intercepting the eastern flank of the SMC a second time on 20 July at 87° E (Fig. 1d). Between 20 and 24 July the time series shows the mixed-layer cooling, increasing in salinity, and deepening to 40 m of depth as barrier layer thickness increases to 40 m (area between two solid black lines; Fig. 6a and b). Surface chlorophyll concentrations are patchy as the float intercepts the SMC, with average mixed-layer chlorophyll concentrations varying daily between 0.1 and 0.4 mg m^{-3} (Fig. 6d). Average values of h_2 are around 16 ± 1 m, varying between 10 and 20 m, which is smaller than the 15 to 31 m sub-daily variability of h_2 observed from the glider in the SMC.

Conversely, observations on the western side of the basin from float 629, between 8 and 11° N, show average h_2 values of 20 m compared with the average h_2 values of 16 m in the SMC from SG579 (Fig. 5a). The time series of chlorophyll concentration from the westernmost float 629 shows the MLD increasing from 25 to 50 m and the deep chlorophyll maximum deepening from 30 to 50 m between 16 July
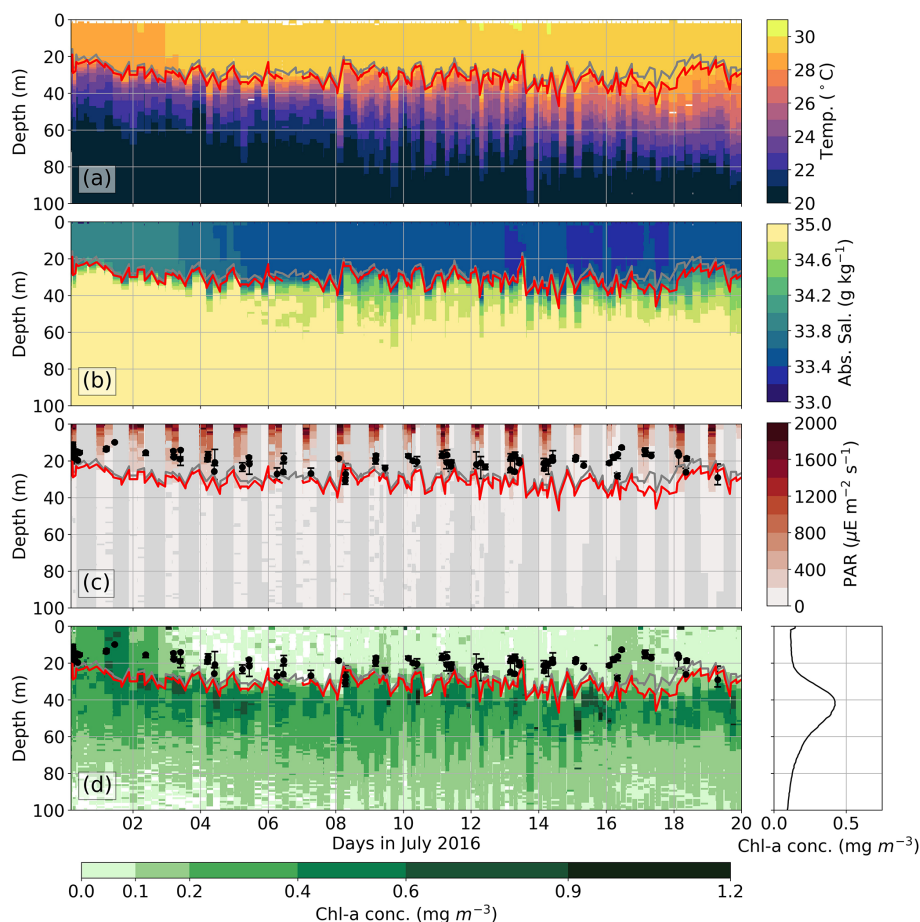
Figure 3. Time series of observations measured by glider SG579, linearly interpolated to 1 m depth intervals down to 100 m: **(a)** temperature (°C), **(b)** absolute salinity (g kg^{-1}), **(c)** PAR (μE m^{-2} s^{-1}), and **(d)** chlorophyll concentration with the vertical profile of the average chlorophyll concentration (mg m^{-3}). The black circles are scale depth values, h_2 (m). The MLD is defined as the depth at which density is same as the surface density plus an increase in density equivalent to a 0.8 °C decrease in temperature, and the isothermal layer depth is calculated as the depth at which temperature is 0.8 °C cooler than SST (Kara et al., 2000; Thushara et al., 2019). The region between the MLD (grey line) and isothermal layer depth (red line) is the barrier layer.

and 13 August (Fig. 7d). Away from the SLD and SMC, float 629 encounters a more transparent upper ocean with increased h_2 and a reduced mixed-layer chlorophyll concentration of 0.2–0.3 mg m^{-3}. Closer to the eastern Indian continental shelf, the influence of the freshwater runoff from rivers entering the basin enhances the supply of biological material and the nutrient supply to the upper water column (Lotliker et al., 2016). Sedimentary material also reduces the solar penetrative depths and increases solar absorption in the surface layers of the coastal region. As float 629 approaches the eastern Indian continental shelf, h_2 is reduced to the west of 83° E (Fig. 5b), likely due to high chlorophyll concentrations and sedimentary material in this region as captured by satellite (Fig. 5a). On 13 September, surface geostrophic velocities from satellite altimetry show an anticyclonic eddy moving eastward away from the eastern Indian coast (not shown) intercepting the path of float 629, causing the mixed layer to shoal and salinity to increase by 0.6 g kg^{-1} in 2 d (Fig. 7b).

Average Chl a_{30} increases to 0.4 mg m^{-3}, and corresponding h_2 values decrease to a minimum of 11 m (Fig. 7d).

Daily variations in salinity of 0.2 g kg^{-1} are observed by float 630 during 6–12 July, with the highest salinity recorded at 34.4 g kg^{-1} in the mixed layer and the barrier layer on 10 July (Fig. 8b), possibly due to eddies shearing off from the main SMC flow (Fig. 1d). Values of h_2 are around 16 m as average Chl a_{30} of $\sim$0.2 mg m^{-3} (Fig. 8d) is entrained by the SMC and advected into the path of float 630 at around 89° E in early July. Towards the end of September at 89° E, the influence of the SMC on chlorophyll concentration decreases as the SMC shifts to the western side of the basin away from float 630 (Fig. 1f), consistent with climatological observations (Webber et al., 2018). Consequently, at 89° E a southeastward flow containing water from the eastern side of the basin along with some recirculated surface water from the SMC is observed (Fig. 1e and f). Float 631 yields h_2 values greater than 20 m (Fig. 6d), possibly indicating that the
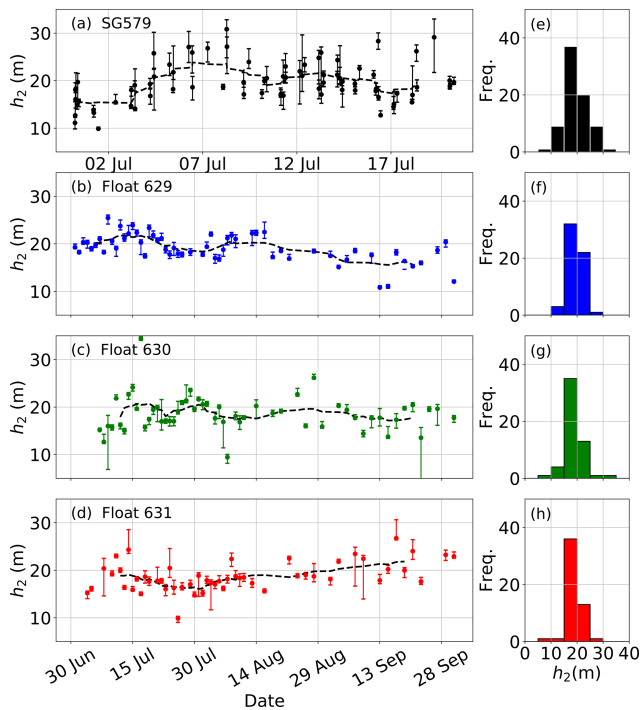
Figure 4. (a–d) Time series of observed h_2: **(a)** glider SG579 (black), **(b)** float 629 (blue), **(c)** float 630 (green), and **(d)** float 631 (red). Dashed black lines represent a centred moving average of h_2 values with a window size of 10 data points. **(e–h)** Histograms of observed h_2 for each glider and floats with the same colour scheme as the time series. The error bars indicate the uncertainty of derived values of h_2.

southeastward flow advects low surface chlorophyll concentrations from the biologically unproductive eastern side of the BoB. We hypothesize that the displacement of the SMC to the western BoB would lead to reduced solar penetration depth in the west and increased solar penetration depth in the east during the summer.

3.2 Relationship between scale depth and chlorophyll concentration

Visible radiation in the upper ocean decreases by approximately 63 % $(1 - e^{-1})$ from the surface to a depth equal to 1 scale depth. Glider observations show that over 80 % of PAR is absorbed to a depth of 30 m (Fig. 3c). The majority of visible radiation is absorbed at the near-surface; hence, the chlorophyll concentration at the near-surface strongly influences the amount of visible radiation absorbed, which strongly influences the radiant heating rate of the ocean surface. We examine the relationship between the average chlorophyll concentration in the surface layer and h_2, both observed by the glider. The average MLD in the glider time series (Fig. 3d) and the determined maximum h_2 are approximately 30 m. Hence, we calculate the average Chl a_{30}. We do not derive a relationship between chlorophyll and h_2
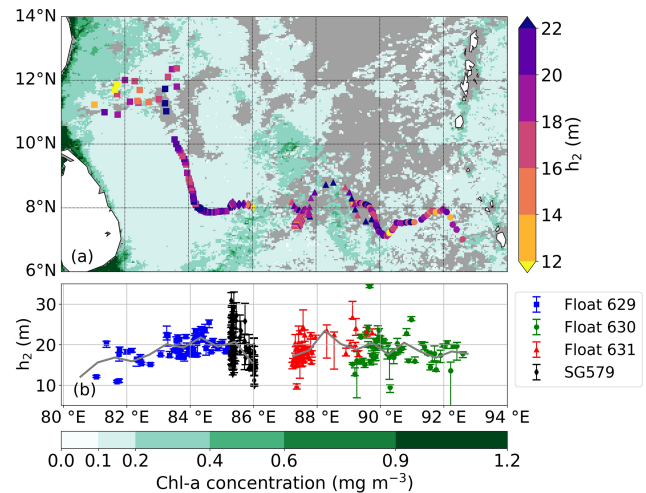
Figure 5. (a) Location of each profile for glider SG579 (diamond), float 629 (square), float 630 (circle), and float 631 (triangle) across the southern Bay of Bengal coloured by the observed h_2 value. The ESA OC-CCI version 3.1 satellite composite of 4 km chlorophyll a concentration for the month of July 2016 is shown. **(b)** The h_2 variability with longitude across the basin for glider SG579 (black diamond), float 629 (blue square), float 630 (green circle), and float 631 (red triangle). The grey solid line represents the mean h_2 value binned at 0.5° intervals.

Table 1. Summary of determination coefficients (r^2) and root mean square errors (RMSEs) when comparing parameterizations to ocean-glider-observed (SG579) scale depth, h_2, and average 0–30 m mixed-layer chlorophyll concentrations (Fig. 9).

Source	Label	r^2	RMSE (m)
Morel and Antoine (1994)	MA94	0.35	3.6
Ohlmann (2003)	O03	0.35	3.7

from the profiling floats, since the float chlorophyll concentration is itself derived from vertical profiles of light absorption ($E_d(490)$).

As expected, h_2 is inversely related to chlorophyll concentration (Fig. 9). Observed average chlorophyll concentrations from glider SG579 vary by a factor of 6 during the BoBBLE campaign. Larger h_2 values of ~ 20 m are associated with lower mixed-layer chlorophyll concentrations of less than 0.3 mg m^{-3}; smaller h_2 values of ~ 12 m are associated with higher mixed-layer chlorophyll concentrations of 0.35 mg m^{-3}.

The observations compare well with two commonly used double exponential parameterizations in ocean GCMs relating light absorption to chlorophyll concentration (Fig. 9; Table 1) from Morel and Antoine (1994) (MA94) and Ohlmann (2003) (O03). We assume for the O03 two-band solar absorption scheme that the incident angle of solar radiation on the ocean surface and the cloud index are both zero. Both the parameterizations define a power-law dependence
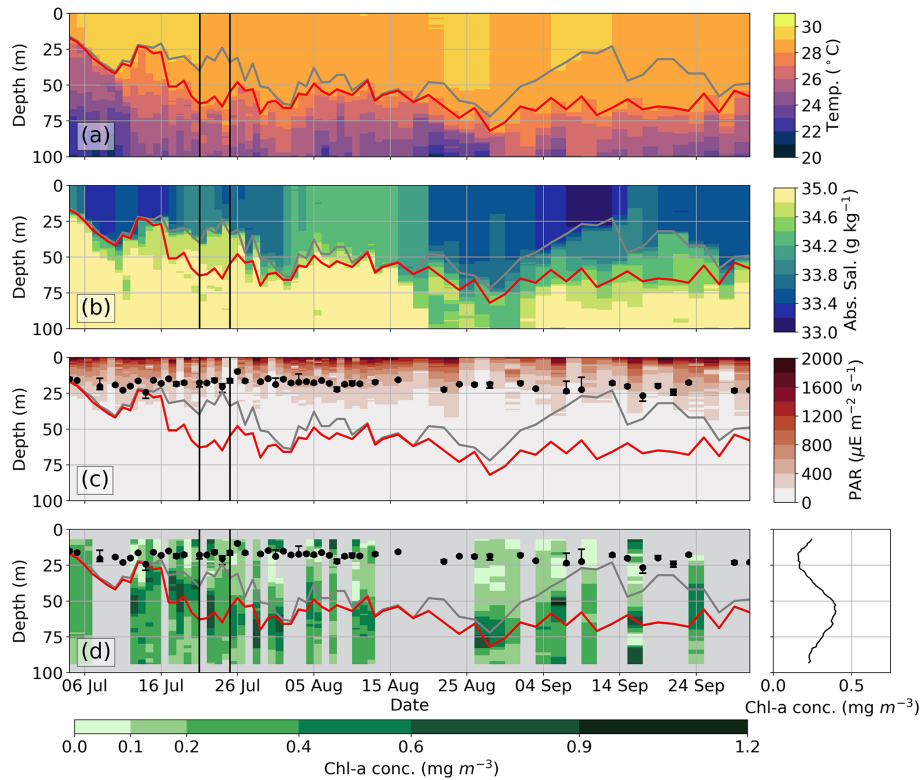
Figure 6. Time series of observations measured by float 631, linearly interpolated to 1 m depth intervals: **(a)** temperature (°C), **(b)** absolute salinity (g kg^{-1}), **(c)** PAR μE m^{-2} s^{-1}, and **(d)** chlorophyll concentration with the vertical profile of the average chlorophyll concentration (mg m^{-3}). Grey sections in the chlorophyll time series represent removed $E_d(490)$ profiles that displayed excessive noise. The black dots are scale depth values, h_2 (m). The region between the MLD (grey line) and isothermal layer depth (red line) is the barrier layer.

on scale depth as a function of chlorophyll, with the greatest change in scale depth occurring at lower chlorophyll concentrations, between 0.08 and 0.1 mg m^{-3}, and the smallest change in scale depth occurring at higher chlorophyll concentrations above 0.2 mg m^{-3} (Fig. 9). The determination coefficients (r^2) of O03 and MA94 against the observations show that these functions fit similarly to determined values of h_2. The parameterizations predict scale depths to be within ± 3.6 m of the determined h_2. For chlorophyll concentrations larger than 0.2 mg m^{-3}, MA94 and O03 predict scale depths smaller than the determined h_2, although the number of observations above this concentration is limited. From our results, we cannot definitively select the most appropriate parameterization given the spread and uncertainty in the h_2 estimates.

3.3 Implications of chlorophyll concentration for BoB SST

The determined values of h_2 for each glider and float time series varies by a factor of 2 (Fig. 4e–h). The 5th and 95th percentile of all h_2 values are 14 and 26 m, respectively. With the majority of solar radiation absorbed in the surface mixed layer, the difference between $h_2 = 14$ and $h_2 = 26$ m would

have significant effects on the radiant heating of the surface layer and SST. We can compare the impact these two values of h_2 would have on the temperature change for an idealized water column. The temperature change is related to the daily average solar radiant heating rate of a layer of upper ocean with thickness H as

$$
\left.\frac{\mathrm{d}T}{\mathrm{d}t}\right|_Q = \frac{Q_{\mathrm{sw}}(0) - Q_{\mathrm{sw}}(H)}{\rho c_p H}
$$
$$
= \frac{Q_{\mathrm{sw}}(0) - (1-R)Q_{\mathrm{sw}}(0)e^{-\frac{z}{h_2}}}{\rho c_p H}, \tag{2}
$$

where we specify $H = 30$ m to represent the average MLD from the glider, $\rho = 1021$ kg m^{-3} to represent the average density of seawater in the upper 30 m from the glider dataset, and $c_p = 3850$ J kg^{-1} K^{-1} to represent the specific heat capacity of seawater. The daily average solar irradiance absorbed in this mixed layer is calculated by taking the difference between the daily average solar irradiance incident on the ocean surface, $Q_{\mathrm{sw}}(0)$, and daily average solar irradiance at the base of the mixed layer, $Q_{\mathrm{sw}}(H)$. At depths greater than 5 m, we assume all red light is absorbed and $Q_{\mathrm{sw}}(H)$ is then the blue-light radiation flux that penetrates the base of the mixed layer.
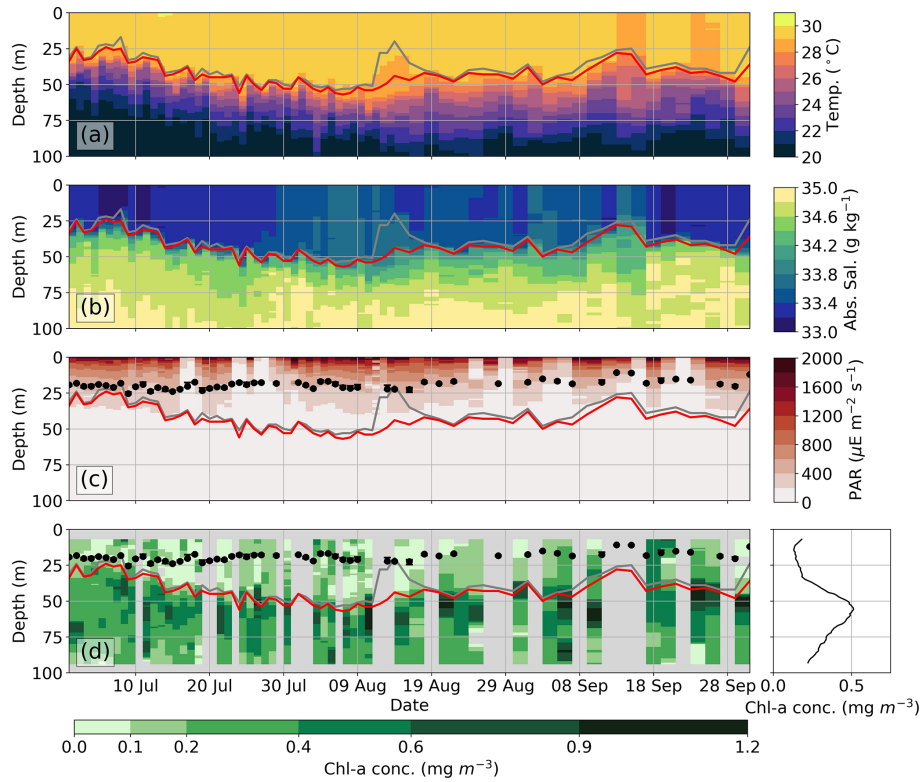
Figure 7. As Fig. 6 but for float 629.
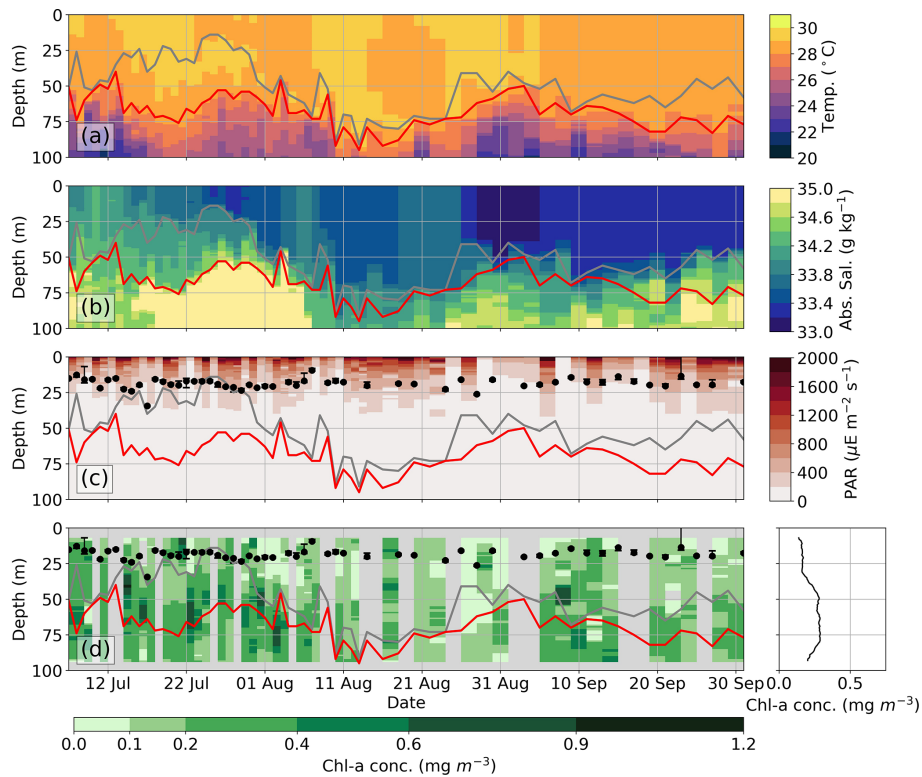
Figure 8. As Fig. 6 but for float 630.
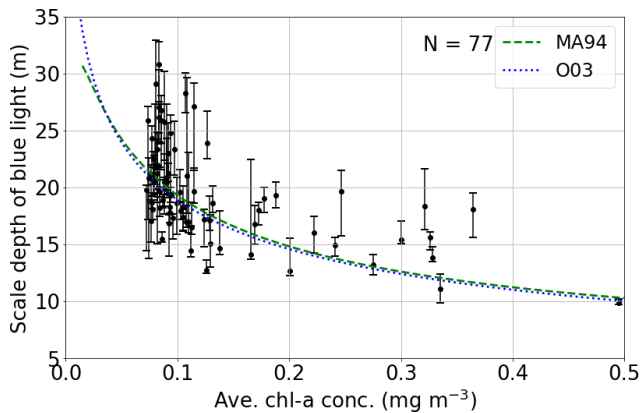
Figure 9. Observed h_2 against average chlorophyll a concentration between the surface and 30 m of depth from glider SG579 (black circles). Parameterizations of the scale depth of blue light (equivalent to h_2) for chlorophyll concentrations between 0 and 0.5 mg m^{-3} are presented with the observational data: Morel and Antoine (1994) (MA94) (dashed green line) and Ohlmann (2003) (O03) (dotted blue line).

The daily average solar irradiance incident on the column surface is estimated to be 280 W m^{-2} based on solar irradiance measurements in clear-sky conditions during the observation period (Vinayachandran et al., 2018). For the purposes of this calculation, we ignore the effects of advection, entrainment, and mixing, as well as any atmospheric feedbacks from changing SST (Vijith et al., 2020). The average determined value of h_2 for July, August, and September is indicative of Jerlov water type IB for which $h_2 = 17$ m (Fig. 4e–h); hence, we use a constant value of $R = 0.67$ for the same Jerlov water type. If the water column has an h_2 value of 26 m, then the solar irradiance absorbed in the upper 30 m would be 251 with 29 W m^{-2} absorbed below 30 m. If the water column has an h_2 value of 14 m, then the solar irradiance absorbed in the upper 30 m would be 269 W m^{-2} with 11 W m^{-2} absorbed below 30 m. Using Eq. (2) the increased absorption of solar irradiance in the mixed layer when h_2 decreases from 26 to 14 m leads to a 0.35 °C per month increase in radiant heating rate, confirming that chlorophyll-induced heating over the determined range of h_2 will lead to significantly different values of SST.

These idealized calculations are now extended to further investigate the influence of near-surface chlorophyll concentrations on SST and heat distribution in the upper ocean. A one-dimensional K-profile parameterization (KPP) model (Large et al., 1994) is used to run five idealized simulations with five constant h_2 values of 14, 17, 19, 21, and 26 m, which represent the 5th, 25th, 50th, 75th, and 95th percentiles of all determined values of h_2 from the glider and floats, respectively, throughout July 2016. The model has a simple two-band solar radiation scheme, identical to Paulson and Simpson (1977), to replicate the transmission of solar radiation in the upper ocean. Initial idealized KPP sen-

sitivity experiments, not presented in this paper, show that the influence of R on SST is not negligible, but the influence of h_2 on SST is the largest out of all optical parameters. Hence, five constant values of R from Paulson and Simpson (1977) are chosen with $R = 0.58$ when $h_2 = 26$ m (Jerlov water type I), $R = 0.62$ when $h_2 = 21$ and 19 m (Jerlov water type IA), $R = 0.67$ when $h_2 = 17$ m (Jerlov water type IB), and $R = 0.77$ when $h_2 = 14$ m (Jerlov water type II). The influence of h_1 on SST is negligible and is fixed at 1 m (Jerlov water type IB) for each of the five idealized simulations. The model MLD is defined as the depth at which the bulk Richardson number is equal to a critical value of 0.3 (Large et al., 1994). Horizontal advection, Ekman pumping, and atmospheric feedbacks are absent from the model by design.

The mean vertical profiles of temperature and salinity from the glider for 1–10 July provide the subsurface (0–1000 m of depth) initial conditions. Hourly solar shortwave flux is derived from the downwelling shortwave radiation observed every 2 min from the RAMA (Research Moored Array for African–Asian–Australian Monsoon Analysis and Prediction; McPhaden et al., 2009) mooring at 8° N, 90° E in the southern BoB approximately 4° E of the glider location. The hourly rainfall data are interpolated from the 3-hourly rainfall rate from the Tropical Rainfall Measuring Mission (TRMM; Huffman et al., 2007) for the same location. The sensible and latent heat fluxes and the surface wind stress are sourced from TropFlux (Kumar et al., 2012) at a daily resolution, which are then linearly interpolated to an hourly resolution. TropFlux is used as it provides an accurate representation of heat fluxes during the boreal summer in the BoB (Sanchez-Franks et al., 2018). Evaporation rates are calculated from the latent heat flux from TropFlux at the same hourly resolution. The model is spun up for 1 month using the surface forcing data for June 2016. For this spin-up period, the scale depth of blue light was fixed at the Jerlov water type IB value of $h_2 = 17$ m. After the spin-up, the model was run through July 2016 in five configurations with h_2 equal to 14, 17, 19, 21, and 26 m.

The BoBBLE campaign took place during a suppressed period of convection or a break phase in the South Asian monsoon. The South Asian monsoon is subject to active–break cycles on sub-seasonal timescales (10 to 30 d) driven by the Boreal Summer Intraseasonal Oscillation (BSISO; Wang and Xie, 1997), which are strongly influenced by air–sea interactions (Sengupta et al., 2001). Associated with this break phase, no precipitation is recorded, and solar shortwave flux remains high during the campaign between 4 and 15 July (Fig. 10b and c), allowing for strong diurnal heating of the ocean surface during this period. By 15 July, precipitation increases (Fig. 10c) as deep atmospheric convection enters the campaign region, marking the transition into an active phase of the BSISO.

In the idealized KPP experiments, changing h_2 from 26 to 14 m led to an increase in daily average SST by 0.35 °C
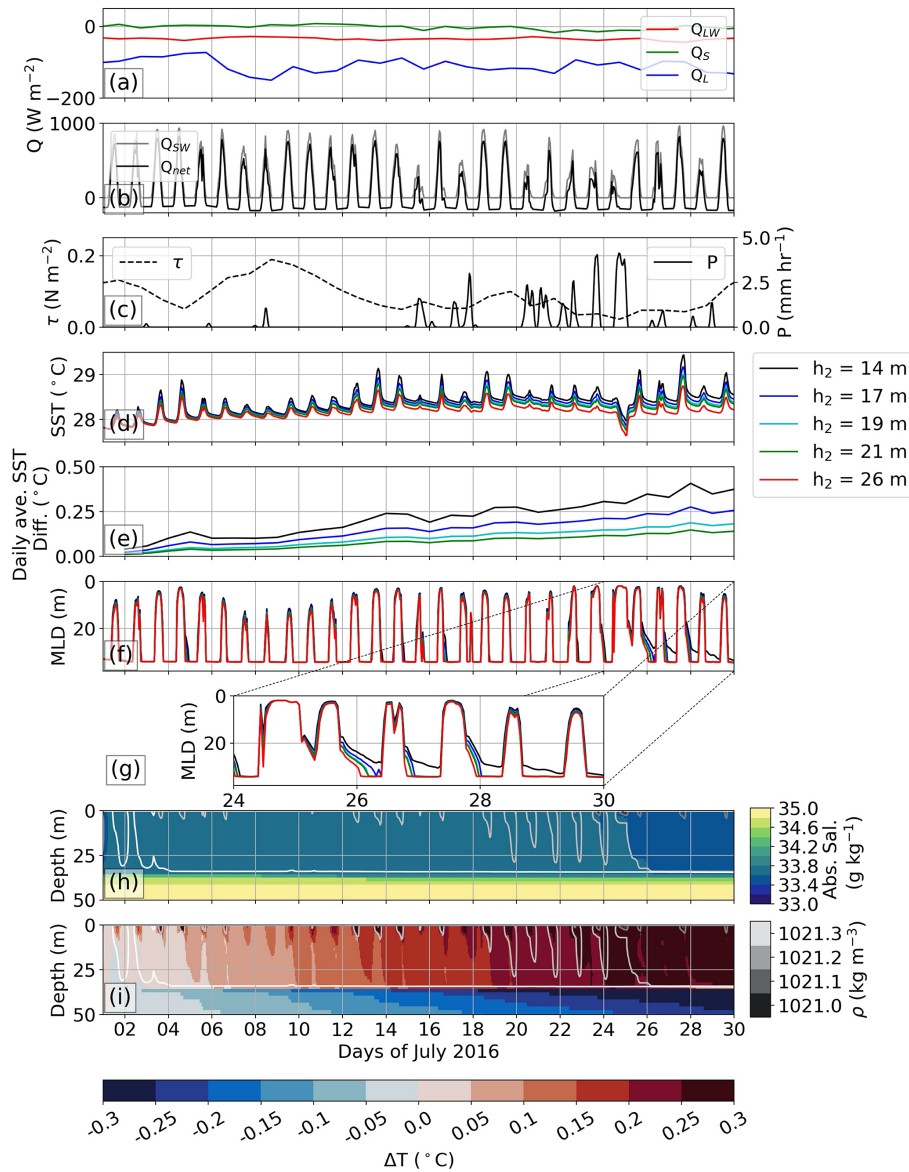
Figure 10. (a) Hourly surface longwave (red line), sensible (green line), and latent (blue line) heat fluxes ($W\,m^{-2}$) for July 2016. **(b)** Hourly surface shortwave (grey line) and net (black line) heat fluxes ($W\,m^{-2}$). **(c)** Wind stress magnitude (dashed black line) ($N\,m^{-2}$) and precipitation rate (solid black line) ($mm\,d^{-1}$). **(d)** Time series of model SST when h_2 is 14 m (black line), 17 m (blue line), 19 m (cyan line), 21 m (green line), and 26 m (red line). **(e)** Time series of daily average SST difference: $SST_{14\,m}$ minus $SST_{26\,m}$ (black line), $SST_{17\,m}$ minus $SST_{26\,m}$ (blue line), $SST_{19\,m}$ minus $SST_{26\,m}$ (cyan line), and $SST_{21\,m}$ minus $SST_{26\,m}$ (green line). **(f)** Time series of model MLD when h_2 is 14 m (black line), 17 m (blue line), 19 m (cyan line), 21 m (green line), and 26 m (red line). **(g)** Time series of model mixed-layer depth between 24 and 30 July. **(h)** Depth–time section of salinity ($g\,kg^{-1}$) and density (contours) ($kg\,m^{-3}$) from the $h_2 = 26$ m simulation. **(i)** Depth–time section of temperature difference ($T_{14\,m} - T_{26\,m}$) (°C) and density (contours) ($kg\,m^{-3}$) from the $h_2 = 26$ m simulation.

within a month (black line; Fig. 10e). The average MLD is 34 m and remains relatively constant during July. Hence, the previous idealized calculation was a good approximation as we estimated a similar amount of radiant heating for a mixed layer of comparable thickness. Decreasing h_2 from 26 to 21, 19, and 17 m leads to progressively larger increases in daily average SST from 0.14, 0.18, and 0.25 °C by the end of July 2016, respectively (Fig. 10e). The maximum diurnal change

in SST for the $h_2 = 14$ m simulation is 1.0 °C compared with 0.62 °C for the $h_2 = 26$ m simulation (Fig. 10d). From 1–15 July the SST from the $h_2 = 14$ m simulation warms at the greatest rate of 0.04 °C d^{-1} compared with 0.02 °C d^{-1} for the $h_2 = 26$ m simulation (Fig. 10d). From 15 July onwards, during an active phase of the BSISO, SST warming for the $h_2 = 14$ m simulation is just 0.01 °C d^{-1} compared with the slight SST cooling in the $h_2 = 26$ m simu-

lation (Fig. 10d). Decreased solar penetration depth leads to increased absorption of solar radiation over a shallower depth of ocean. Hence, the mixed layer warms and the water below the mixed layer cools as less solar radiation penetrates deeper in the water column (Fig. 10i).

On 25 July, high precipitation rates of $4\,\mathrm{mm\,d^{-1}}$ freshen the ocean surface (Fig. 10h), which contributes to an increase in mixed-layer salinity stratification and a reduction in the maximum MLD in all five simulations (Fig. 10f and g). A reduction in wind stress also partly contributes to the reduction in the maximum MLD, as wind-driven turbulent mixing is reduced (Fig. 10c). The mixed layer in the $h_2 = 26\,\mathrm{m}$ simulation shoals to a maximum depth of $30\,\mathrm{m}$ and recovers to a previous depth of $34\,\mathrm{m}$ a day later (Fig. 10f and g). Conversely, the mixed layer in the $h_2 = 14\,\mathrm{m}$ simulation shoals to a maximum depth of $23\,\mathrm{m}$ and recovers to a previous depth of $34\,\mathrm{m}$ 5 d later (Fig. 10f and g). Decreased solar penetration depth and increased solar radiation absorption further increase mixed-layer thermal stratification and stability, which amplifies and prolongs the vertical and temporal change in MLD. Shoaling the mixed layer to a depth comparable to the solar penetration depth increases the sensitivity of SST to changes in chlorophyll concentration (Turner et al., 2012; Giddings et al., 2020). Hence, freshwater input through precipitation and additional biological warming through the occurrence of high chlorophyll concentrations in the SMC and SLD region would enhance SST increase during an active BSISO phase, which would potentially have a positive impact on atmospheric convection.

4 Discussion and conclusions

Observed and inferred chlorophyll concentrations show a deep chlorophyll maximum at 50 to $80\,\mathrm{m}$ across the southern BoB during the southwest monsoon, with higher near-surface chlorophyll concentrations occurring intermittently within the SMC, SLD, and coastal regions. The average h_2 for July, August, and September is indicative of Jerlov water type IB ($h_2 = 17\,\mathrm{m}$). The h_2 values display temporal and spatial variability on sub-daily timescales as a consequence of sub-daily variability of surface chlorophyll concentrations entrained by the SMC. In the SLD and SMC, where high surface chlorophyll concentrations are advected into the southern BoB, h_2 is generally lower. The bifurcation of the SMC, and hence of the chlorophyll entrained in its flow, reduces h_2 values to the south and east of the SMC as filaments and eddies break off from the main current. Away from the SMC, the upper ocean is more transparent, with h_2 values of more than $20\,\mathrm{m}$. In coastal regions, h_2 values are occasionally reduced to $11\,\mathrm{m}$ due to high surface chlorophyll concentrations, as well as other chlorophyll pigments, detritus material, and other biological constituents.

This study has shown that gliders and floats are suitable oceanographic platforms to determine h_2 from observed PAR profiles. PAR profiles measured by the glider tended to be noisier than those measured by the floats. The removal of excessively noisy PAR measurements in the top 5 m means the fit of Eq. (1) to PAR profiles is not constrained at the surface, so the optical parameters of red light are not constrained. Instead, fixed water type IB values of R and h_1 are used to replicate red-light absorption in the top 5 m of all PAR profiles, with a minimal influence on the determined values of h_2 below 5 m. This demonstrates that solar penetration depths for blue light can be determined from in-water PAR profiles measured from gliders and floats without near-surface PAR measurements and without the need for labour-intensive and costly ship-based tethers, CTD rosettes, and buoys used in previous studies (e.g. Ohlmann et al., 1998; Lotliker et al., 2016).

The O03 and MA94 scale depth parameterizations demonstrate similar correlation and RMSE when compared with determined h_2 values and average Chl a_{30}. Both parameterizations demonstrate a power-law relationship of scale depth as a function of chlorophyll and predict scale depths to be within $\pm 3.6\,\mathrm{m}$ of the determined h_2, although both tend to underestimate h_2 for chlorophyll concentrations of 0.2–$0.5\,\mathrm{mg\,m^{-3}}$. The spread and uncertainty of the determined h_2 mean we cannot robustly select the most appropriate parameterization to predict scale depth in this region.

The relationship between determined h_2 and observed chlorophyll concentrations measured from the glider has limitations. Determined h_2 represents not only the attenuation of blue light due to chlorophyll a concentration, but also the attenuation of blue light due to other biological constituents and other suspended particles. Furthermore, the observed chlorophyll concentration is only a proxy for the actual chlorophyll a concentration. Hence, determined h_2 values potentially overestimate blue light attenuation due to chlorophyll a pigments, affecting the relationship between determined h_2, average observed chlorophyll concentration, and the fit of MA94 and O03 shown in Sect. 3.2. Future climate modelling studies should consider different types and concentrations of biological constituents that affect h_2, such as coloured dissolved organic matter (e.g. Kim et al., 2018).

Relatively low blue-light scale depths are likely to occur within the SMC and SLD due to the higher surface chlorophyll concentrations that will in turn lead to locally enhanced warming. The width of the SMC is approximately $300\,\mathrm{km}$ (Webber et al., 2018), and surface chlorophyll begins to increase in April and typically peaks in July (Lévy et al., 2007), resulting in a considerable area and duration of enhanced biological surface warming. Likewise, the eastern and western BoB coastal regions also display smaller solar penetration depths, further widening the region impacted by biological surface warming.

The additional biological warming is likely to be non-uniform across the basin and subject to variability during the summer season. As identified by the observations from the glider and float 631, the SMC contains patches of greater sur-

face chlorophyll within the main flow and within the eddies and filaments that split off from the SMC. The chlorophyll concentration within the SMC depends on its strength and location, which affect the entrainment of phytoplankton from the coastal region of Sri Lanka (Vinayachandran et al., 2004). The SMC strength and location are influenced by the strength of the SLD and the propagation of Rossby waves from the eastern side of the basin (Webber et al., 2018). Hence, if conditions are conducive for a strong SMC intercepting the biologically productive coastal regions from June to July, then the surface chlorophyll concentration increases and enhances surface warming. The SLD also fluctuates in strength and position depending on the local wind stress curl and the propagation of Rossby waves (Webber et al., 2018). Variability in SLD peak strength determines the upwelling of nutrients to the sunlit layers that sustain high surface chlorophyll concentrations (Thushara et al., 2019). Hence, this would vary solar penetration depths and periods of enhanced surface warming in the SLD throughout the summer.

The enhanced surface warming during a 15 d break phase in the BSISO, as shown from the $h_2 = 14$ m simulation, demonstrates the influence that high surface chlorophyll concentrations could have on SST intraseasonal variability (10–30 d timescales). The intraseasonal SST anomalies during the start of the BoBBLE campaign (1–15 July) are $\sim 0.6\,°C$ (Vinayachandran et al., 2018), and previous studies have found the June–July intraseasonal SST variability to be less than $1\,°C$ (Duncan and Han, 2009; Vinayachandran et al., 2012). Our simulations suggest that higher surface chlorophyll (decreasing h_2 to 14 m) could generate an SST perturbation equal to $\sim 60\,\%$ of the intraseasonal SST variability that is observed during the first half of the BoBBLE campaign. This is a significant modulation of SST and underlines the importance of accounting for near-surface chlorophyll and its variability in studies of the BSISO.

KPP is a one-dimensional model and neglects horizontal advection. Submesoscale frontal and eddy activity in the BoB creates sharp horizontal and vertical gradients in temperature and salinity (Ramachandran et al., 2018; Jaeger and Mahadevan, 2018). Strong seasonal surface currents, such as the SMC, advect different water masses, forming fronts and eddies that are continually moving and changing around the BoB. This submesoscale dynamical variability is not replicated in the one-dimensional KPP model. However, for the purposes of this paper, the simplicity inherent in not representing three-dimensional dynamics means that the results of our chlorophyll sensitivity experiments are unambiguous.

The modulation of SST by biological warming has important feedbacks to the South Asian monsoon system. Imposing seasonally varying chlorophyll concentrations in the BoB has been shown to increase rainfall up to $3\,\mathrm{mm\,d^{-1}}$ over Myanmar during the southwest monsoon onset and over Bangladesh during the autumn intermonsoon (Giddings et al., 2020). However, little is known about the impact of chlorophyll concentration on the intraseasonal variability of summer monsoon rainfall. The SST intraseasonal variability is strongly coupled to active and break periods of the BSISO (Fu et al., 2003), and it even partly contributes to the northward and northwestward propagation of convective bands (Gao et al., 2018). The $h_2 = 14$ m simulation showed increased warming of the ocean surface and hence a more rapid recovery of SST anomalies during the BSISO break period. This would increase the turbulent heat fluxes to the atmosphere, destabilize the atmospheric boundary layer, and potentially trigger convection for the following active period sooner. Glider observations in this study have shown that h_2 ranges between 10 and 31 m on submesoscales and that the sub-seasonal temporal variability of h_2 strongly depends on the strength and positioning of the SMC and SLD. Hence, the timing and spatial scale of the chlorophyll blooms in the central BoB relative to the break periods of the BSISO are additional factors to consider when modelling intraseasonal convective events.

Appendix A: Determining in situ chlorophyll *a* concentration from downwelling irradiance

This Appendix provides a description of the method, key assumptions, and quality control process used to derive a proxy for in situ chlorophyll *a* concentration from downwelling irradiance at 490 nm measured by the Argo profiling floats.

Downward irradiance, E_d, at wavelength λ decays approximately exponentially as it penetrates through the water column. The irradiance just below the surface, $E_d(\lambda, -0)$, decays with depth, z, at each discretized layer, dz, from the surface, 0, to z. The rate of decay of irradiance, defined as the diffuse attenuation coefficient, $K_d(\lambda, z)$, is allowed to vary in each discretized layer of 1 m thickness. The function is given as

$$\ln E_d(\lambda, z) = \ln E_d(\lambda, -0) - \sum_1^n K_d(\lambda, z)\, \Delta z, \qquad (A1)$$

where $K_d(\lambda, z)$ is defined as the sum of the attenuation of pure seawater (K_w) and the attenuation due to biological material (K_{bio}). For each discretized layer, K_w is assumed to remain constant, but K_{bio} is allowed to vary in order to derive depth-varying chlorophyll *a* concentration profiles. K_{bio} varies as a non-linear power-law function of the chlorophyll *a* concentration (Chl *a*) (Morel, 1988; Morel and Maritorena, 2001), meaning that $K_d(\lambda)$ is defined as

$$K_d(\lambda) = K_w(\lambda) + \chi(\lambda)\, [\text{Chl } a]^{e(\lambda)}, \qquad (A2)$$

where $\chi(\lambda)$ and $e(\lambda)$ are empirically determined coefficients. Equation (A1) then becomes

$$\ln E_d(\lambda, z) = \ln E_d(\lambda, -0)$$
$$- \sum_1^n \left[K_w(\lambda) + \chi(\lambda)\, [\text{Chl } a]^{e(\lambda)} \right] \Delta z. \qquad (A3)$$

Morel et al. (2007) derived the spectrally dependent $\chi(\lambda)$ and $e(\lambda)$ parameters using linear regression analysis of the log-transformed chlorophyll *a* concentration and K_d sourced from the LOV (Laboratoire d'Océanographie de Villefranche) dataset. This study used optical parameters $K_w(490) = 0.0166$, $\chi(\lambda) = 0.08253$, and $e(\lambda) = 0.6529$ for wavelength 490 nm. Measured irradiance values $\ln E_d(490, z)$ and $\ln E_d(490, -0)$ (Fig. A1a) are used to determine K_{bio} for each discretized layer using Eq. (A3) (Fig. A1b and c; black dotted line). Further quality control is applied to remove smaller "cloud" spikes (caused by the transient passage of clouds across the sun) from profiles of K_{bio}, which is identified as a large anomalous alternating positive and negative spikes. K_{bio} values that are above a threshold of $0.1\,\text{m}^{-1}$ and below $-0.05\,\text{m}^{-1}$ are also removed. The profiles are linearly interpolated onto a 1 m grid, and a centred rolling median of window size 15 is applied to smooth over any remaining anomalous noise (Fig. A1c; magenta dotted line). Chlorophyll concentrations are calculated using $\chi(\lambda)$ and $e(\lambda)$ (Fig. A1d; green dotted line).

The relationship between light absorption and chlorophyll *a* concentration is assumed to be constant, and open-ocean water in the southern BoB is assumed to be categorized as "case 1" waters with optical properties affected by chlorophyll pigments and detrital organic matter (Morel, 1988). The BoB surface ocean mainly consists of chlorophyll *a* pigments, as shown from in situ water samples (Madhu et al., 2006), chlorophyll *a* fluorescence measurements, and remotely sensed satellite measurements (Thushara et al., 2019). Hence, Eq. (A3) and the empirically determined coefficients are suitable to determine chlorophyll *a* concentration profiles from $E_d(490)$ measured by the floats.
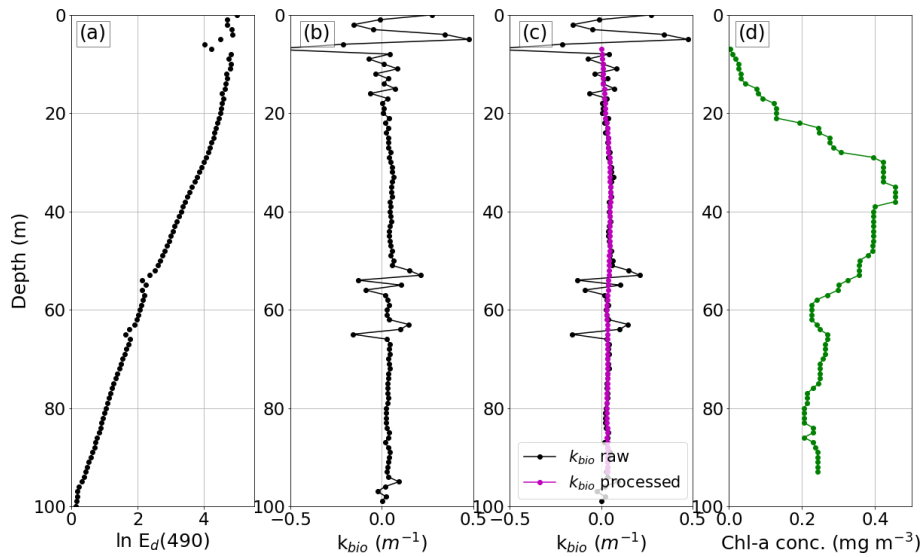
Figure A1. (a) Profile of ln $E_\mathrm{d}(490)$ from dive 10, float 631, interpolated onto a 1 m vertical grid. **(b)** The attenuation due to biological constituents, K_bio (m^{-1}). **(c)** K_bio (m^{-1}) before quality control processing (black dotted line) and after quality control processing (magenta dotted line). **(d)** Chlorophyll a concentration (mg m^{-3}) (green dotted line).

References

Argo: Argo float data and metadata from Global Data Assembly Centre (Argo GDAC), SEANOE, https://doi.org/10.17882/42182, 2018.

BODC: British Oceanographic Data Centre, OceanGlider Data Assembly Centre, available at: https://www.bodc.ac.uk/data/bodc_database/gliders/, last access: 2 September 2019.

Copernicus: Marine Environment Monitoring Service, available at: https://marine.copernicus.eu/, last access: 15 August 2018.

Drushka, K., Sprintall, J., and Gille, S. T.: Subseasonal variations in salinity and barrier-layer thickness in the eastern equatorial Indian Ocean, J. Geophys. Res.-Oceans, 119, 805–823, https://doi.org/10.1002/2013JC009422, 2014.

Duncan, B. and Han, W.: Indian Ocean intraseasonal sea surface temperature variability during boreal summer: Madden-Julian Oscillation versus submonthly forcing and processes, J. Geophys. Res., 114, C05002, https://doi.org/10.1029/2008JC004958, 2009.

Fu, X., Wang, B., Li, T., and McCreary, J. P.: Coupling between northward-propagating, intraseasonal oscillations and sea surface temperature in the Indian Ocean, J. Atmos. Sci., 60, 1733–1753, https://doi.org/10.1175/1520-0469(2003)060<1733:CBNIOA>2.0.CO;2, 2003.

Gao, Y., Klingaman, N. P., DeMott, C. A., and Hsu, P.-C.: Diagnosing ocean feedbacks to the BSISO: SST-modulated surface fluxes and the moist static energy budget, J. Geophys. Res.-Atmos., 124, 146–170, https://doi.org/10.1029/2018JD029303, 2018.

Giddings, J., Matthews, A. J., Klingaman, N. P., Heywood, K. J., Joshi, M., and Webber, B. G. M.: The effect of seasonally and spatially varying chlorophyll on Bay of Bengal surface ocean properties and the South Asian monsoon, Weather Clim. Dynam., 1, 635–655, https://doi.org/10.5194/wcd-1-635-2020, 2020.

Girishkumar, M. S., Joseph, J., Thangaprakash, V. P., Pottapinjara, V., and McPhaden, M. J.: Mixed layer temperature budget for the northward propagating summer monsoon intraseasonal oscillation (MISO) in the central Bay of Bengal, J. Geophys. Res.-Oceans, 122, 8841–8854, https://doi.org/10.1002/2017JC013073, 2017.

Gordon, H. R. and McCluney, W. R.: Estimation of the depth of sunlight penetration in the sea for remote sensing, Appl. Opt., 14, 413–416, https://doi.org/10.1364/AO.14.000413, 1975.

Huffman, G. J., Adler, R. F., Bolvin, D. T., Gu, G. J., Nelkin E. J., Bowman, K. P., Hoong, Y., Stocker, E. F., and Wolff, D. B.: The TRMM multisatellite precipitation analysis (TMPA): Quasi-global, multiyear, combined-sensor precipitation estimates at fine scales, J. Hydrometeorol., 8, 38–55, https://doi.org/10.1175/JHM560.1, 2007.

IOC, SCOR, and IAPSO: The international thermodynamic equation of seawater – 2010: Calculation and use of thermodynamic properties, Intergovernmental Oceanographic Commission, Manuals and Guides Number 56, available at: http://www.teos-10.org/pubs/TEOS-10_Manual.pdf (last access: 20 May 2019), UNESCO, 196 pp., 2010.

Jaeger, G. S. and Mahadevan, A.: Submesoscale-selective compensation of fronts in a salinity-stratified ocean, Sci. Adv., 4, e1701504, https://doi.org/10.1126/sciadv.1701504, 2018.

Jensen, T. G.: Cross-equatorial pathways of salt and tracers from the northern Indian Ocean: Modelling results, Deep-

Sea Res. Pt. II, 50, 2111–2127, https://doi.org/10.1016/S0967-0645(03)00048-1, 2003.

Jerlov, N. G.: Optical oceanography, Oceanography Series 5, Elsevier Publishing Company, Amsterdam, Netherlands, 193 pp., 1968.

Kara, A. B., Rochford, P. A., and Hurlburt, H. E.: An optimal definition for ocean mixed layer depth, J. Geophys. Res.-Oceans, 105, 16803–16821, https://doi.org/10.1029/2000JC900072, 2000.

Kay, J. E., Deser, C., Phillips, A., Mai, A., Hannay, C., Strand, G., Arblaster, J. M. Bates, S. C., Danabasoglu, G., Edwards, J., Holland, M., Kushner, P., Lamarque, J.-F., Lawrence, D., Lindsay, K., Middleton, A., Munoz, E., Neale, R., Oleson, K., Polvani, L., and Vertenstein, M.: The Community Earth System Model (CESM) large ensemble project: A community resource for studying climate change in the presence of internal climate variability, B. Am. Meteorol. Soc., 96, 1333–1349, https://doi.org/10.1175/BAMS-D-13-00255.1, 2015.

Kim, G. E., Gnanadesikan, A., DelCastillo, C. E., and Pradal, M.-A.: Upper ocean cooling in a coupled climate model due to light attenuation by yellowing materials, Geophys. Res. Lett., 45, 6134–6140, https://doi.org/10.1029/2018GL077297, 2018.

Kumar, B. P., Vialard, J., Lengaigne, M., Murty, V. S. N., and Mcphaden, M. J.: TropFlux: air-sea fluxes for the global tropical oceans – description and evaluation, Clim. Dynam., 38, 1521–1543, https://doi.org/10.1007/s00382-011-1115-0, 2012.

Large, W. G., McWilliams, J. C., and Doney, S. C.: Oceanic vertical mixing: A review and a model with a nonlocal boundary layer parameterization, Rev. Geophys., 32, 363–403, https://doi.org/10.1029/94RG01872, 1994.

Lavender, S., Jackson, T., and Sathyendranath, S.: The ocean colour climate change initiative, Ocean Challenge, 21, 29–31, available at: https://climate.esa.int/en/projects/ocean-colour/ (last access: 4 July 2018), 2015.

Lee, Z.-P., Darecki, M., Carder, K. L., Davis, C. O., Stramski, D., and Rhea, W. J.: Diffuse attenuation coefficient of downwelling irradiance: An evaluation of remote sensing methods, J. Geophys. Res.-Oceans, 110, C02017, https://doi.org/10.1029/2004JC002573, 2005.

Lengaigne, M., Menkes, C., Aumont, O., Gorgues, T., Bopp, L., André, J.-M., and Madec, G.: Influence of the oceanic biology on the tropical Pacific climate in a coupled general circulation model, Clim. Dynam., 28, 503–516, https://doi.org/10.1007/s00382-006-0200-2, 2007.

Lévy, M., Shankar, D., André, J.-M., Shenoi, S. S. C., Durand, F., and de Boyer Montégut, C.: Basin-wide seasonal evolution of the Indian Ocean's phytoplankton blooms, J. Geophys. Res.-Oceans, 112, C12014, https://doi.org/10.1029/2007JC004090, 2007.

Lewis, M. R., Carr, M.-E., Feldman, G. C., Esaias, W., and McClain, C.: Influence of penetrating solar radiation on the heat budget of the equatorial Pacific Ocean, Nature, 347, 543–545, https://doi.org/10.1038/347543a0, 1990.

Li, Y., Han, W., Wang, W., Ravichandran, M., Lee, T., and Shinoda, T.: Bay of Bengal salinity stratification and Indian summer monsoon intraseasonal oscillation: 2. Impact on SST and convection, J. Geophys. Res.-Oceans, 122, 4312–4328, https://doi.org/10.1002/2017JC012692, 2017.

Lotliker, A. A., Omand, M. M., Lucas, A. J., Laney, S. R., Mahadevan, A., and Ravichandran, M.: Penetrative radiative flux in the Bay of Bengal, Oceanogr., 29, 214–221, https://doi.org/10.5670/oceanog.2016.53, 2016.

Madhu, N. V., Jyothibabu, R., Maheswaran, P. A., John Gerson, V., Gopalakrishnan, T. C., and Nair, K. K. C.: Lack of seasonality in phytoplankton standing stock (chlorophyll a) and production in the western Bay of Bengal, Cont. Shelf Res., 26, 1868–1883, 2006.

McPhaden, M. J., Meyers, G., Ando, K., Masumoto, Y., Murty, V. S. N., Ravichandran, M., Syamsudin, F., Vialard, J., Yu, L., and Yu, W.: RAMA: The research moored array for African-Asian-Australian monsoon analysis and prediction, B. Am. Meteorol. Soc., 90, 459–480. https://doi.org/10.1175/2008BAMS2608.1, 2009.

Mignot, J., Swingedouw, D., Deshayes, J., Marti, O., Talandier, C., Séférian, R., Lengaigne, M., and Madec, G.: On the evolution of the oceanic component of the IPSL climate models from CMIP3 to CMIP5: A mean state comparison, Ocean Model., 72, 167–184, https://doi.org/10.1016/j.ocemod.2013.09.001, 2013.

Morel, A.: Optical modeling of the upper ocean in relation to its biogenous matter content (case I waters), J. Geophys. Res.-Oceans, 93, 10749–10768, https://doi.org/10.1029/JC093iC09p10749, 1988.

Morel, A. and Antoine, D.: Heating rate within the upper ocean in relation to its bio-optical state, J. Phys. Oceanogr., 24, 1652–1665, https://doi.org/10.1175/1520-0485(1994)024<1652:HRWTUO>2.0.CO;2, 1994.

Morel, A., Huot, Y., Gentili, B., Werdell, P. J., Hooker, S. B., and Franz, B. A.: Examining the consistency of products derived from various ocean color sensors in open ocean (Case 1) waters in the perspective of a multi-sensor approach, Remote Sens. Environ., 111, 69–88, https://doi.org/10.1016/j.rse.2007.03.012, 2007.

Morel, A. and Maritorena, S.: Bio-optical properties of oceanic waters: A reappraisal, J. Geophys. Res.-Oceans, 106, 7163–7180, https://doi.org/10.1029/2000JC000319, 2001.

Müller, P., Li, X.-P., and Niyogi, K. K.: Non-photochemical quenching. A response to excess light energy, Plant Physiol., 125, 1558–1566, https://doi.org/10.1104/pp.125.4.1558, 2001.

Murtugudde, R., Beauchamp, J., McClain, C. R., Lewis, M., and Busalacchi, A. J.: Effects of penetrative radiation on the upper tropical ocean circulation, J. Climate, 15, 470–486, https://doi.org/10.1175/1520-0442(2002)015<0470:EOPROT>2.0.CO;2, 2002.

Nakamoto, S., Kumar, S. P., Oberhuber, J. M., Muneyama, K., and Frouin, R.: Chlorophyll modulation of sea surface temperature in the Arabian Sea in a mixed-layer isopycnal general circulation model, Geophys. Res. Lett., 27, 747–750, https://doi.org/10.1029/1999GL002371, 2000.

Ohlmann, J. C.: Ocean radiant heating in climate models, J. Climate, 16, 1337–1351, 2003.

Ohlmann, J. C. and Siegel, D. A.: Ocean radiant heating. Part II: Parameterizing solar radiation transmission through the upper ocean, J. Phys. Oceanogr., 30, 1849–1865, 2000.

Ohlmann, J. C., Siegel, D. A., and Washburn, L.: Radiant heating of the western equatorial Pacific during TOGA-COARE, J. Geophys. Res.-Oceans, 103, 5379–5395, 1998.

Organelli, E., Claustre, H., Bricaud, A., Schmechtig, C., Poteau, A., Xing, X., Prieur, L., D'Ortenzio, F., Dall'Olmo, G., Vellucci, V.: A novel near-real-time quality-control procedure

for radiometric profiles measured by Bio-Argo floats: protocols and performances, J. Atmos. Ocean. Tech., 33, 937–951, https://doi.org/10.1175/JTECH-D-15-0193.1, 2016.

Paulson, C. A. and Simpson, J. J.: Irradiance measurements in the upper ocean, J. Phys. Oceanogr., 7, 952–956, https://doi.org/10.1175/1520-0485(1977)007%3C0952:IMITUO%3E2.0.CO;2, 1977.

Ramachandran, S., Tandon, A., Mackinnon, J., Lucas, A. J., Pinkel, R., Waterhouse, A. F., Nash, J., Shroyer, E., Mahadevan, A., Weller, R. A. and Farrar, J. T.: Submesoscale processes at shallow salinity fronts in the Bay of Bengal: Observations during the winter monsoon, J. Phys. Oceanogr., 48, 479–509, 2018.

Sager, J. C. and McFarlane, J. C.: Radiation, in: Plant Growth Chamber Handbook, edited by: Langhans R. W. and Tibbitts T. W., available at: https://www.controlledenvironments.org/wp-content/uploads/sites/6/2017/06/Ch01.pdf (last access: 16 July 2020), Iowa State Univ. Press., Iowa State Univ., Iowa, USA, 1–29, 1997.

Sanchez-Franks, A., Kent, E. C., Matthews, A. J., Webber, B. G. M., Peatman, S. C., and Vinayachandran, P. N.: Intraseasonal variability of air-sea fluxes over the Bay of Bengal during the southwest monsoon, J. Climate, 31, 7087–7109, https://doi.org/10.1175/JCLI-D-17-0652.1, 2018.

Sanchez-Franks, A., Webber, B. G. M., King, B. A., Vinayachandran, P. N., Matthews, A. J., Sheehan, P. M. F., Behara, A., and Neema, C. P.: The railroad switch effect of seasonally reversing currents on the Bay of Bengal high-salinity core, Geophys. Res. Lett., 46, 6005–6014, https://doi.org/10.1029/2019GL082208, 2019.

Sathyendranath, S., Grant, M., Brewin, R. J. W., Brockmann, C., Brotas, V., Chuprin, A., Doerffer, R., Dowell, M., Farman, A., Groom, S., Jackson, T., Krasemann, H., Lavender, S., Martinez Vicente, V., Mazeran, C., Mélin, F., Moore, T.S., Müller, D., Platt, T., Regner, P., Roy, S., Steinmetz, F., Swinton, J., Valente, A., Zühlke, M., Antoine, D., Arnone, R., Balch, W. M., Barker, K., Barlow, R., Bélanger, S., Berthon, J.-F., Beşiktepe, Ş., Brando, V. E., Canuti, E., Chavez, F., Claustre, H., Crout, R., Feldman, G., Franz, B., Frouin, R., García-Soto, C., Gibb, S. W., Gould, R., Hooker, S., Kahru, M., Klein, H., Kratzer, S., Loisel, H., McKee, D., Mitchell, B. G., Moisan, T., Muller-Karger, F., O'Dowd, L., Ondrusek, M., Poulton, A. J., Repecaud, M., Smyth, T., Sosik, H. M., Taberner, M., Twardowski, M., Voss, K., Werdell, J., Wernand, M., and Zibordi, G.: ESA Ocean Colour Climate Change Initiative (Ocean_Colour_cci): Version 3.1 Data, Centre for Environmental Data Analysis [data], https://doi.org/10.5285/9c334fbe6d424a708cf3c4cf0c6a53f5, 2018.

Sengupta, D., Bharath Raj, G. N., Ravichandran, M., Sree Lekha, J., and Papa, F.: Near-surface salinity and stratification in the north Bay of Bengal from moored observations, Geophys. Res. Lett., 43, 4448–4456, https://doi.org/10.1002/2016GL068339, 2016.

Sengupta, D., Goswami, B. N., and Senan, R.: Coherent intraseasonal oscillations of ocean and atmosphere during the Asian summer monsoon, Geophys. Res. Lett., 28, 4127–4130, https://doi.org/10.1029/2001GL013587, 2001.

Smith, R. C. and Baker, K. S.: Optical properties of the clearest natural waters (200–800 nm), Appl. Opt., 20, 177–184, https://doi.org/10.1364/AO.20.000177, 1981.

Smith, R., Jones, P., Briegleb, B., Bryan, F., Danabasoglu, G., Dennis, J., Dukowicz, J., Eden, C., Fox-Kemper, B., Gent, P., Hecht, M., Jayne, S., Jochum, M., Large, W., Lindsay, K., Maltrud, M., Norton, N., Peacock, S., Vertenstein, M., and Yeager, S.: The parallel ocean program (POP) reference manual ocean component of the community climate system model (CCSM), available at: http://www.cesm.ucar.edu/models/cesm1.0/pop2/doc/sci/POPRefManual.pdf (last access: 4 February 2019), Rep. LAUR-01853, 141, 1–140, 2010.

SSALTO/Duacs: DT all-sat-merged Global Ocean Gridded SSALTO/DUACS Sea Surface Height L4 product and derived variables, available at: https://www.aviso.altimetry.fr/en/home.html, last access: 15 August 2018.

Sweeney, C., Gnanadesikan, A., Griffies, S. M., Harrison, M. J., Rosati, A. J., and Samuels, B. L.: Impacts of shortwave penetration depth on large-scale ocean circulation and heat transport, J. Phys. Oceanogr., 35, 1103–1119, https://doi.org/10.1175/JPO2740.1, 2005.

Thomalla, S. J., Moutier, W., Ryan-Keogh, T. J., Gregor, L., and Schütt, J.: An optimized method for correcting fluorescence quenching using optical backscattering on autonomous platforms, Limnol. Oceanogr., 16, 132–144, https://doi.org/10.1002/lom3.10234, 2018.

Thushara, V., Vinayachandran, P. N. M., Matthews, A. J., Webber, B. G. M., and Queste, B. Y.: Vertical distribution of chlorophyll in dynamically distinct regions of the southern Bay of Bengal, Biogeosciences, 16, 1447–1468, https://doi.org/10.5194/bg-16-1447-2019, 2019.

Turner, A. G., Joshi, M., Robertson, E. S., and Woolnough, S. J.: The effect of Arabian Sea optical properties on SST biases and the South Asian summer monsoon in a coupled GCM, Clim. Dynam, 39, 811–826, https://doi.org/10.1007/s00382-011-1254-3, 2012.

Vialard, J., Foltz, G. R., McPhaden, M. J., Duvel, J. P., and de Boyer Montégut, C.: Strong Indian Ocean sea surface temperature signals associated with the Madden-Julian Oscillation in late 2007 and early 2008, Geophys. Res. Lett., 35, L19608, https://doi.org/10.1029/2008GL035238, 2008.

Vijith, V., Vinayachandran, P. N., Webber, B. G., Matthews, A. J., George, J. V., Kannaujia, V. K., Lotliker, A. A., and Amol, P.: Closing the sea surface mixed layer temperature budget from in situ observations alone: Operation Advection during BoBBLE, Sci. Rep., 10, 7062, https://doi.org/10.1038/s41598-020-63320-0, 2020.

Vinayachandran, P. N., Chauhan, P., Mohan, M., and Nayak, S.: Biological response of the sea around Sri Lanka to summer monsoon, Geophys. Res. Lett., 31, L01302, https://doi.org/10.1029/2003GL018533, 2004.

Vinayachandran, P. N., Matthews, A. J., Vijay Kumar, K., Sanchez-Franks, A., Thushara, V., George, J, Vijith, V., Webber, B. G. M., Queste, B. Y., Roy, R., Sarkar, A., Baranowski, D. B., Bhat, G. S., Klingaman, N. P., Peatman, S. C., Parida, C., Heywood, K. J., Hall, R., King, B., Kent, E. C., Nayak, A. A., Neema, C. P., Amol, P., Lotliker, A., Kankonkar, A., Gracias, D. G., Vernekar, S., D'Souza, A. C., Valluvan, G., Pargaonkar, S. M., Dinesh, K., Giddings, J., and Joshi, M.: BoBBLE (Bay of Bengal Boundary Layer Experiment): Ocean–atmosphere interaction and its impact on the South Asian monsoon, B. Am. Meteorol. Soc., 99, 1569–1587, https://doi.org/10.1175/BAMS-D-16-0230.1, 2018.

Vinayachandran, P. N., Murty, V. S. N., and Ramesh Babu, V.: Observations of barrier layer formation in the Bay of Bengal during summer monsoon, J. Geophys. Res.-Oceans, 107, 8018, https://doi.org/10.1029/2001JC000831, 2002.

Vinayachandran, P. N. and Yamagata, T.: Monsoon response of the sea around Sri Lanka: Generation of thermal domes and anticyclonic vortices, J. Phys. Oceanogr., 28, 1946–1960, https://doi.org/10.1175/1520-0485(1998)028<1946:MROTSA>2.0.CO;2, 1998.

Vinayachandran, P. N., Neema, C. P., Mathew, S., and Remya, R.: Mechanisms of summer intraseasonal sea surface temperature oscillations in the Bay of Bengal, J. Geophys. Res.-Oceans, 117, C01005, https://doi.org/10.1029/2011JC007433, 2012.

Wang, B. and Xie, X.: A model for the boreal summer intraseasonal oscillation, J. Atmos. Sci., 54, 72–86, https://doi.org/10.1175/1520-0469(1997)054<0072:AMFTBS>2.0.CO;2, 1997.

Webber, B. G. M., Matthews, A. J., Vinayachandran, P. N., Neema, C. P., Sanchez-Franks, A., Vijith, V., Amol, P., and Baranowski, D. B.: The dynamics of the southwest monsoon current in 2016 from high-resolution in situ observations and models, J. Phys. Oceanogr., 48, 2259–2282, https://doi.org/10.1175/JPO-D-17-0215.1, 2018.

Wetzel, P., Maier-Reimer, E., Botzet, M., Jungclaus, J., Keenlyside, N., and Latif, M.: Effects of ocean biology on the penetrative radiation in a coupled climate model, J. Climate, 19, 3973–3987, https://doi.org/10.1175/JCLI3828.1, 2006.

Xing, X., Morel, A., Claustre, H., Antoine, D., D'Ortenzio, F., Poteau, A., and Mignot, A.: Combined processing and mutual interpretation of radiometry and fluorimetry from autonomous profiling Bio-Argo floats: Chlorophyll a retrieval, J. Geophys. Res.-Oceans, 116, C06020, https://doi.org/10.1029/2010JC006899, 2011.

Zaneveld, J. R. V., Kitchen, J. C., and Pak, H.: The influence of optical water type on the heating rate of a constant depth mixed layer, J. Geophys. Res.-Oceans, 86, 6426–6428, https://doi.org/10.1029/JC086iC07p06426, 1981.

Zaneveld, J. R. V., Boss, E., and Barnard, A.: Influence of surface waves on measured and modeled irradiance profiles, Appl. Opt., 40, 1442–1449, https://doi.org/10.1364/AO.40.001442, 2001.